Ahmad, Saeed; Mustonen, Kimmo; McLean, Ben; Jiang, Hua; Zhang, Qiang; Hussain, Aqeel; Khan, Abu Taher; Ding, Er Xiong; Liao, Yongping; Wei, Nan; Monazam, Mohammad R.A.; Nasibulin, Albert G.; Kotakoski, Jani; Page, Alister J.; Kauppinen, Esko I.

Hybrid Low-Dimensional Carbon Allotropes Formed in Gas Phase

Published in:
Advanced Functional Materials

DOI:
10.1002/adfm.202005016

Published: 04/11/2020

Document Version
Publisher's PDF, also known as Version of record

ADVANCED FUNCTIONAL MATERIALS
www.afm-journal.de

Hybrid Low-Dimensional Carbon Allotropes Formed in Gas Phase

Saeed Ahmad, Kimmo Mustonen, Ben McLean, Hua Jiang, Qiang Zhang,* Aqeel Hussain, Abu Taher Khan, Er-Xiong Ding, Yongping Liao, Nan Wei, Mohammad R. A. Monazam, Albert G. Nasibulin, Jani Kotakoski, Alister J. Page, and Esko I. Kauppinen**

Graphene, carbon nanotubes (CNTs) and fullerenes are the basic set of low-dimensional carbon allotropes. The latter two arise from the former by selective removal and addition of carbon atoms. Nevertheless, given their morphological disparities, the production of each is typically devised from entirely different starting points. Here, it is demonstrated that all three allotropes can nucleate from (pseudo-)spherical, nanometer-sized transition metal clusters in a gas-suspension when the chemical conditions are favorable. The experimental results indicate that graphitic carbon embryos nucleate on the catalyst particles and sometimes transform into 2D graphene flakes through chain polymerization of carbon fragments forming in the surround gas atmosphere. It is further shown that hydrogenation reactions play an essential role by stabilizing the emerging flakes by mitigating the pentagon and heptagon defects that lead into evolution of fulleroids. Ab initio molecular dynamics simulations show that the ratio of hydrogen to carbon in the reaction is a key growth parameter. Since structural formation takes place in a gas-suspension, graphene accompanied by fullerenes and single-walled CNTs can be deposited on any surface at ambient temperature with arbitrary layer thicknesses. This provides a direct route for the production and deposition of graphene-based hybrid thin films for various applications.

1. Introduction

Graphene is the thinnest imaginable material consisting only of a single layer of carbon atoms. Breaking the curse laid down by the Mermin–Wagner theorem nearly a half-century earlier, it was isolated from graphite using the famous Scotch-tape method in 2004.[1] Despite having been subject to rigorous theoretical work long before this hallmark event,[2] it was, at the time,[3] the last experimentally realized low-dimensional carbon allotrope. Fullerenes were discovered in the 1980's[4] and carbon nanotubes (CNTs) in the 1990's.[5] Owing to its unusual electronic structure, which gives rise to ballistic charge transport,[6] superconductivity in twisted bilayers[7] and many other fascinating quantum phenomena,[8,9] it has become the foundation of what are now dubbed as the 2D van der Waals (vdW) heterostructures, or the "atomic Lego."[10] Although not nearly as extensively studied, fullerenes, and nanotubes have been in the past assembled into 1D vdW heterostructures known as carbon peapods,[11] and much more recently incorporated into mixed-dimensional, vertically-assembled vdW stacks.[12–16] Being more reactive than graphene, covalent links between the molecules have been devised in chemical synthesis to form a carbon nanobud structure[17] that has been further manipulated using high-energy electron irradiation.[18]

The formation of fullerenes, single-walled CNTs (SWCNTs) and graphene have been studied in situ in electron microscopes.[15,19,20] These experiments, in which graphene has never

Dr. S. Ahmad, Dr. H. Jiang, Dr. Q. Zhang, Dr. A. Hussain, A. T. Khan, Dr. E.-X. Ding, Dr. Y. Liao, Dr. N. Wei, Prof. E. I. Kauppinen
Department of Applied Physics
Aalto University School of Science
P.O. Box 15100, Aalto FI-00076, Finland
E-mail: qiang.zhang@aalto.fi; esko.kauppinen@aalto.fi

The ORCID identification number(s) for the author(s) of this article can be found under https://doi.org/10.1002/adfm.202005016.

DOI: 10.1002/adfm.202005016

Dr. K. Mustonen, Dr. M. R. A. Monazam, Prof. J. Kotakoski
Faculty of Physics
University of Vienna
Boltzmanngasse 5, Vienna 1090, Austria
E-mail: kimmo.mustonen@univie.ac.at

Dr. B. McLean, Prof. A. J. Page
School of Environmental and Life Sciences
the University of Newcastle
Callaghan, NSW 2308, Australia

Prof. A. G. Nasibulin
Skolkovo Institute of Science and Technology
Moscow, Russia

Prof. A. G. Nasibulin
Department of Chemistry and Materials Science
Aalto University School of Chemical Engineering
P.O. Box 16100, Aalto FI-00076, Finland

been witnessed emerging from a spherical catalyst, or nanotubes from a planar substrate, has led to a view that their formation mechanisms and kinetics are fundamentally different. Indeed, the seminal CNT growth-chirality theory predicted no correlation between the catalyst symmetry and the emerging tube structure.[21] Essentially the same conclusion can be drawn based on the plane interface theory that considers the catalyst as a solid bulk surface.[22] Meanwhile, some authors have reported that the catalyst symmetry—especially for solid-alloy catalysts[23]—determines the emerging SWCNTs structures.[24] Considering the epitaxial relationship of graphene growing on metal surfaces,[25,26] this train of thought also appears perfectly justified. The old ideas (based on catalyst symmetry), however, along with the development of advanced computational models accounting for the nanotube structural selectivity (if any) to statistical properties in the catalyst-nanotube interface,[27,28] have now come under more scrutiny. Experiments conducted along the same lines have failed to support the role of the catalyst, but rather implicate the emerging nanotube properties largely on external factors, such as the composition of the surrounding gas atmosphere.[29,30] We have previously studied SWCNT structural control based on the reaction balance of carbon monoxide (CO) and dioxide (CO_2) in a floating catalyst process[31] similar to this work. These results support the interpretation that both SWCNT diameter and chiral angle depend sensitively on the chemical environment. Finally, graphene of relatively poor quality has been synthesized from alcohol vapor exposed to microwave plasma in the complete absence of catalyst.[32] The success of this approach, which bears a superficial resemblance to plasma enhanced synthesis of carbon nanotubes,[33] places the templated formation of sp^2 carbon under a certain amount of suspicion.

Here, we present nucleation and growth experiments with ethylene (C_2H_4) exposed to (pseudo-)spherical catalyst nanoparticles formed from transition metals using a floating catalyst system. We show that in conventional chemical vapor deposition (CVD) operated at the limit of the self-pyrolysis temperature of the carbon source, the catalyst remains instrumental for the nucleation of low-dimensional carbon allotropes, but turns out to be somewhat irrelevant in terms of their internal structure and morphology. Instead, with a rigorous set of experiments, we establish that high-quality graphene, along with carbon nanotubes and fullerenes, can emerge from such clusters. Supported by molecular dynamics (MD) simulations we propose a mechanism in which, prior to catalytic nucleation on the clusters, graphene flakes grow rapidly through chain polymerization of sp^2 carbon fragments forming in the surrounding gas atmosphere and finally become detached from the catalyst. While the emergence of carbon nanotubes and fullerenes in similar synthesis conditions is commonplace, the formation of graphene has not been reported.

2. Results and Discussions

2.1. Experimental Set-Up and Material Deposition

The experiments were conducted using an in-house built floating catalyst CVD (FC-CVD) system,[30,34] which was earlier developed to study SWCNT formation and aggregation.[35] The catalyst nanoparticles are formed in a spark discharge generator (SDG) under a nitrogen (N_2) atmosphere and introduced to the CVD reactor (see **Figure 1**a). This unconventional approach enables the size and concentration of nanoparticles to be determined by external means. Here we used a differential mobility analyzer (Nano-DMA, Grimm Aerosol Technik, Germany)—a widely adopted method in aerosol research—to categorize the size (and concentration) of gas-suspended particles based on their drag-limited drift velocities in a strong electric field.[36,37] The size distribution of the particles used in these experiments can be found in the Supporting Information. The distributions are also shown for the CVD products where this is relevant for interpretation. In the following, we will mainly cite the (geometric) mean diameters of the distributions, with occasional references to related concentrations. For synthesis we used 200 ppm of C_2H_4 as the carbon source in a mixture of N_2 and hydrogen (H_2) with their respective volumetric% range from 74–90 to 26–10. The CVD temperature was set to 1050 °C with a total gas flow rate of 0.5 lpm measured at ambient temperature. For spectroscopic characterization of the reactor products were sampled on fibrous nitrocellulose films and press-transferred onto suitable solid substrates.[38] For electron and atomic force microscopy the reaction products were deposited directly on suitable microscopy supports using thermophoresis.[39] More exhaustive details of the synthesis and deposition are given in the Experimental Section and technical descriptions in references.[30,34,40]

2.2. Morphology and Growth Mechanism

The overall morphology of the as-synthesized graphene and carbon nanotube network is shown in Figure 1b. This, and the subsequent images were acquired with a scanning transmission electron microscope (STEM) medium angle annular dark field (MAADF) detector at a 60 keV electron energy. The sample imaged for Figure 1b was supported on a carbon film, but for better stability, subsequent frames were captured on a perforated silicon nitride film with 200 nm holes. For better visibility of the atomic structure, the STEM samples were cleaned with a 10 ms, 600 mW laser pulse in UHV conditions prior to imaging.[41] The samples in Figures 1,2 were synthesized using 3.0 nm iron (Fe) catalysts (size distribution in Figure S1, Supporting Information) and 16 volume% of H_2.

Depending on how the graphene flakes were wrapped on the SWCNTs, they either display the appearance of an "axe" (Figure 1c), "sail" (Figure 1d), or "scroll" (Figure 1e). The scrolls fold upon themselves several times, but sails and axes usually only once. Figure 1f shows an example of monolayer graphene wrapping around a tube ≈9.9 Å in diameter to form a vdW pocket at the edge of a sail. We analyzed the stacking and structure of the molecules by translating the image into reciprocal space through Fourier transform, as shown in Figure 1g. Based on measurement in reciprocal space, the chiral angle of the tube is ≈21° and thus, the chiral indices are (9,5). The graphene envelope is randomly oriented around the tube wall, as can be seen from the rotational mismatch of SWCNT layer lines (L_x) and graphene reflections,[16] although the top and the bottom layers are mutually aligned. The random stacking-order is in

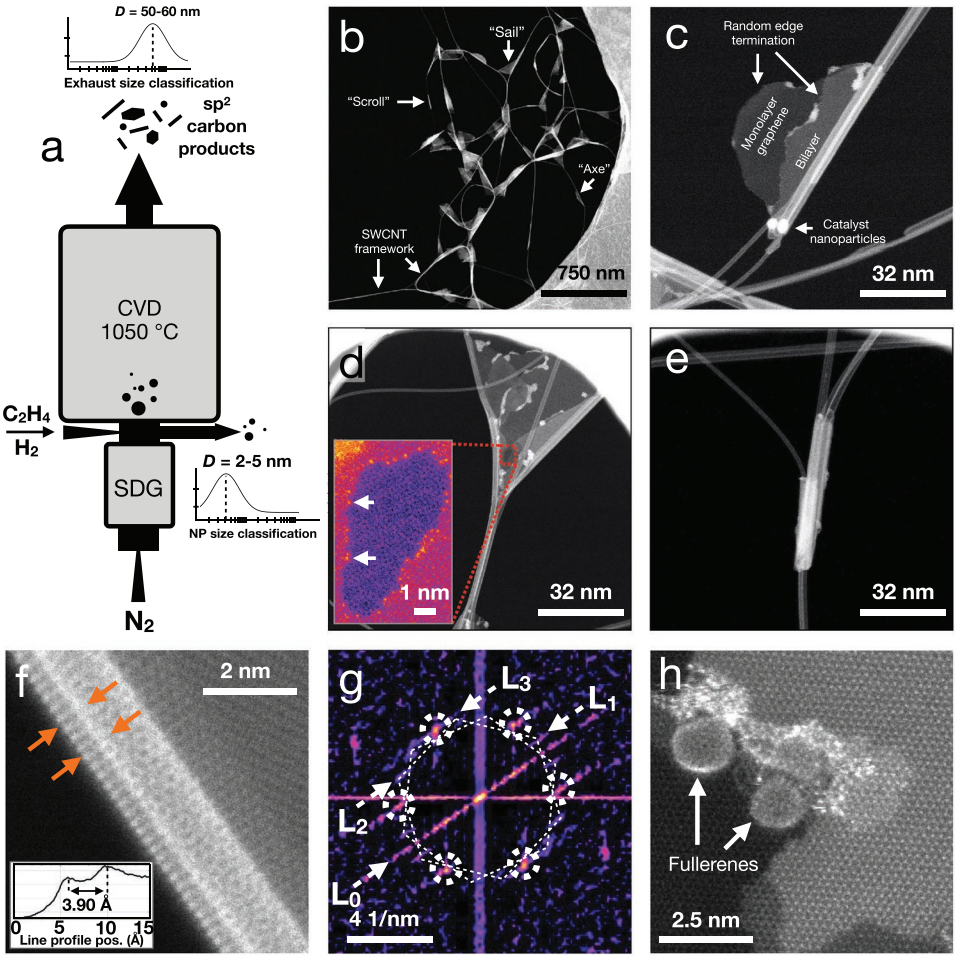

Figure 1. Synthesis and morphology of the material. a) A schema of the synthesis process. The nanoparticles (NPs) are formed in a spark discharge generator (SDG) and their size distribution is determined before the CVD furnace and the low-dimensional carbon allotropes are synthesized from C_2H_4 in the presence of size-classified NPs. The abbreviation "D" in the schema stands for the geometric mean sizes of the particles and CVD product. b) A scanning transmission electron microscope (STEM) medium angle annular dark field (MAADF) overview image of the reaction products showing their general morphology. c–e) Examples of low-magnification STEM images of graphene flakes wrapping around SWCNTs to form "axes," "sails," and "scrolls", respectively. The inset in panel (d) shows the graphene edge termination. The bright atoms at the edges are mostly silicon (identification in Figure S2, Supporting Information). f) A (9,5) SWCNT wrapped in monolayer graphene to form a van der Waals (vdW) pocket. The inset shows an intensity profile over the molecular interface with a vdW gap of 3.9 Å. g) A reciprocal space presentation of the vdW structure in (f). The six circled parts are the graphene first order reflections and the arrowed L_x lines are diffraction layer lines from the SWCNT. h) Fullerenes immobilized on graphene. All images were acquired at 60 kV electron energy and the image contrast of (d) inset and (g) was improved by applying the ImageJ lookup table "fire".

agreement with the measured 3.9 Å vdW spacing (Figure 1f inset), which is about 15% larger than expected for AB-stacked graphene.[42] From time to time we also observed fullerenes stuck at the graphene edges (Figure 1h). These molecules had diameters of about 1–2 nm, similar to those of experimentally observed SWCNTs (see the spectroscopic characterization in Figure S4, Supporting Information). They must be covalently bound to graphene (or the amorphous material), since otherwise the high energy electrons or even thermal fluctuations would have displaced them.[43]

At the atomic scale the structure of the 2D flakes is similar to that of any substrate grown CVD graphene. Monolayers, however, cover clearly less than half of the total surface area on most observed flakes. The average thickness of sail-type flakes, for example, was 3–4 layers, but up to six layers were observed in some cases (Figure S3, Supporting Information). We suspect that the flakes typically grow either in a mono- or few-layer configuration and form thicker layers upon deposition, which we shall discuss later on. Figures 2a,b show a representative monolayer area with an expected threefold covalent structure. The image was captured from a larger flake shown in Figure S3, Supporting Information, where also the exact position is indicated. No visible lattice defects[44] are observed within the field of view, except for a single Fe impurity that is highlighted in the left bottom corner (elemental identification can be found from Supporting Information). Since the atom was trapped on a stacked part of the sample, the bonding configuration could not be determined.

Selected area electron diffraction (SAED) was used to determine the average C—C bond length in the suspended flakes. This was done by finding the lengths of the reciprocal primitive vectors $\boldsymbol{b}_1$ and $\boldsymbol{b}_2$ (Figure 2c) that are mathematically

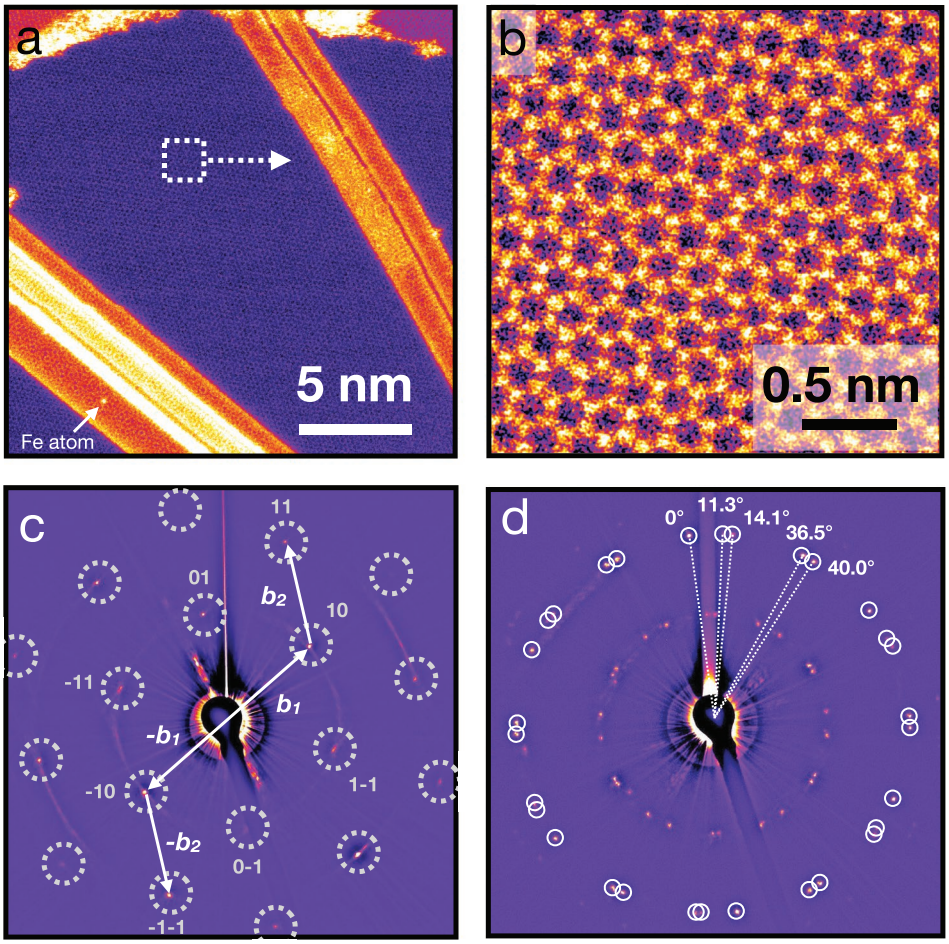

Figure 2. The atomic structure of graphene flakes. a) A STEM image showing a clean monolayer area on a large sail-type graphene flake suspended on several SWCNTs (the entire structure can be seen in Figure S3, Supporting Information). b) An atomically resolved closeup from the center. c) A selected area electron diffraction pattern (SAED, aperture size 0.17 µm) collected under parallel illumination from an individual graphene flake. The graphene reciprocal primitive vectors b_1 and b_2 are indicated. d) A SAED pattern from a turbostratic few-layer graphene with diffraction contributions visible from at least five separate layers. For clarity, the second order diffraction spots are encircled and their rotational mismatch angles are indicated.

related to the real space dimensions of the graphene unit cell. The stacking angles of the graphene multi-layers were random, and we could not establish any general preference based on the diffraction patterns (see example in Figure 2d). The mean C—C bond length was 1.44 ± 0.01 Å based on the average of several diffraction patterns. This value is fairly close to the commonly accepted 1.42 Å, with the small difference likely emerging from the (positive) strain caused by wrapping around the carbon nanotubes.[16] The graphene edge termination had no preference towards either zigzag or armchair configurations, but was entirely random. This is evident from, for example, the uneven edge shape in Figure 1c,d,h and from Figure S3, Supporting Information. The reactive edge-atoms were often decorated with impurity species that appear brighter in the STEM images due to an atomic weight greater than that of carbon (magnified in Figure 1d). Some of these atoms were identified as silicon (Si, see Supporting Information), which we believe must have diffused in after the growth and possibly from the TEM supports used in the experiments.[45]

We next turn our attention away from the structural analysis and discuss the formation of the observed carbon allotropes. Since nucleation of graphene in free-space (from non-hydrocarbon sources[32]) has neither been reported by others nor witnessed by us, we investigated the role of hydrogen in this process using ab initio MD simulations (see Section 4). These simulations show that carbon network condensation as a result of ethylene decomposition is controlled by the H:C ratio present in the reaction environment.[46–48] These simulations are performed in the absence of a metal catalyst, as the role of H during the nucleation of carbon nanotubes[49] and graphene[50] on metal catalysts such as Fe is well established. Here, the simulations investigate the role H plays in the formation of carbon fragments and ring networks in the atmosphere surrounding the catalyst. **Figure 3** presents representative carbon fragments obtained after 500 ps for H:C ratios between 0 (i.e., carbon-only) and 2 (i.e., fully saturated). Due to a slightly lower formation energy of non-hexagonal carbon rings, the deficiency in hydrogen increased their frequency and incorporation into the carbon networks (the statistics are

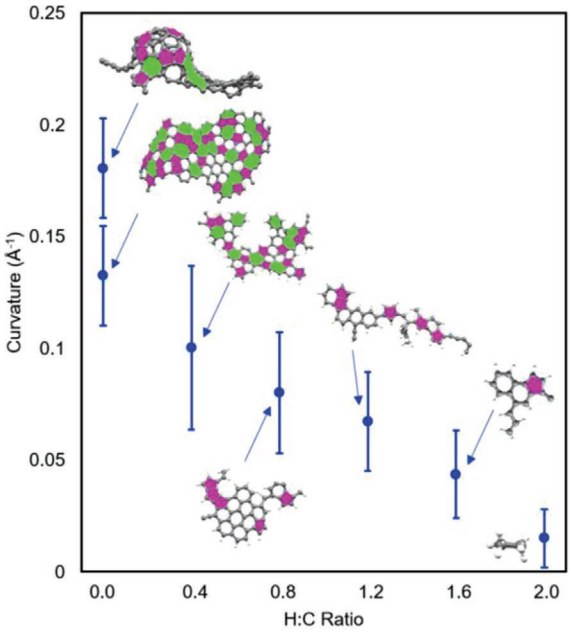

Figure 3. Formation of graphitized carbon fragments. Molecular dynamics results of ethylene (C_2H_4) decomposition and carbon network formation at varying H:C ratios. The fragments forming at H:C < 1 are rich in pentagon defects and thus have a structure comparable to that of fullerenes or carbon nanotube endcaps. The highest likelihood for growth of extended hexagonal carbon structures is observed at ≈H:C = 1; this ratio balances the structure's ability to grow while healing defects in its structure. Higher H:C ratios also result in planar hexagonal structures, but at slower growth rates. The simulation cell was a 3 nm cube with an initial specific density of 170. The temperature was 1050 °C.

shown in Figure S8, Supporting Information). These defects were predominantly pentagon rings and to a lesser extent heptagons. The incorporation of pentagon defects into the carbon network induces a positive curvature leading to the formation of fulleroids, as can be seen in Figure 3. The mechanism through which these structures further convert into fullerene molecules (and possibly into carbon nanotubes) is well established.[51,52] At an intermediate hydrogen supply (H:C ratio of 0.8–1.2), topological defects such as pentagons and heptagons are less likely to remain kinetically trapped. This drives the formation of more planar, structurally pristine carbon networks that grow at a slower rate. In addition, hydrogen rapidly etches away the lower stability configurations at the edges and promotes the formation of hexagonal fragments of a smaller size.[46] If the H:C ratio is further increased beyond 1.6, the network formation is kinetically impeded by hydrogen passivating the carbon dangling bonds at the edges.

Based on the simulation results we initially postulated that under a certain (although a priori unknown) H:C ratio, hexagonal carbon fragments would nucleate and grow independently without a catalyst in gas-suspension. A similar mechanism had been proposed for the formation of polycyclic aromatic hydrocarbons[46] and for cloned SWCNTs.[53] In experiments, however, we were unable to establish any conditions where, without the catalyst, solid carbon formations above the detection threshold of our aerosol measurement could have been detected (Figure S5, Supporting Information).

In the subsequent experiments, the hydrogen concentration was varied and the standard 3.0 nm Fe catalyst was introduced in the CVD reactor. When H_2 supply was either significantly increased or decreased around the established optimal value (at 16 vol% of H_2), a reduced graphene yield was observed (**Figure 4**a–c). This also appeared to negatively affect the overall size of the flakes, although due to the relatively small sample size, the statistical relevance of this result remains uncertain. The size distributions are shown in Figure 4 insets. Increasing H_2 supply from 10 to 24 vol% affected the carbon feed rate to the catalysts by inhibiting the non-catalytic formation of acetylene (C_2H_2) in the reactor, as gauged by its concentration dropping from ≈30 to ≈10 ppm in the exhaust gas. More reactive than the ethylene precursor, it is a likely transitional step in the formation of smaller hydrocarbon fragments,[54] which may precede the formation of the sub-nanometer-sized carbon fragments seen in the simulations. The C_2H_2 concentration was analyzed by Fourier transform infrared (FTIR) gas chromatography as explained in the Supporting Information and depicted in Figure S9, Supporting Information. The H_2 concentration did not appreciably affect the diameter of the SWCNTs. However, based on Raman spectroscopic signatures, tube crystallinity had a strong positive correlation with the H_2 feed rate (see spectroscopic characterization in Supporting Information). Similar to $CO \rightleftarrows CO_2$ equilibrium reactions,[55] we believe this is a manifestation of non-graphitic carbon being etched through the hydrogenation of the most reactive atomic sites, as predicted by the ab initio MD results shown in Figure 3. The hypothesis is also supported by a clear increase in methane production at higher H_2 concentrations, likely a result of greater hydrogenation rate (Figure S9, Supporting Information). Although we did not address the tube atomic structure systematically in this work, our previous experiments indicate that the inclusion of ppm levels of water vapor in an ethylene-based process[56] also reduces the frequency of topological defects that are being incorporated into SWCNT walls (see Figure S10, Supporting Information).

Despite being frequently encapsulated in SWCNT endcaps, catalysts attached to graphene flakes were not commonplace. One rare example of such a catalyst is shown in **Figure 5**, reproduced with two contrast settings to highlight different parts. The left image shows an elliptical cross-section of the particle itself with major and minor axes of 3.7 and 2.9 nm in length, respectively. The dimensions are fairly close to the mean size of 3.0 nm determined with the DMA. A partially enclosed carbon shell is visible in the lower part of the image and is emphasized either with dashed lines (Figure 5a) or arrows (Figure 5b). The demarcation between the carbon shell and the surrounding graphene appears to cease to exist in the top half of the image, which is magnified in Figure 5c. The apparent brightness variation between the atomic sites is likely due to ABA-stacked triple layer graphene disappearing on the monolayer area shown in Figure 5d.

Since graphene flakes were mainly found in connection with SWCNTs, but almost never in contact with catalysts, the possibility that they grow as one could not be immediately excluded. Although this certainly can happen occasionally, the observations conducted using an atomic force microscope (AFM, see Section 4) show that is not exclusively the case. For these experiments, the samples were deposited on mica by

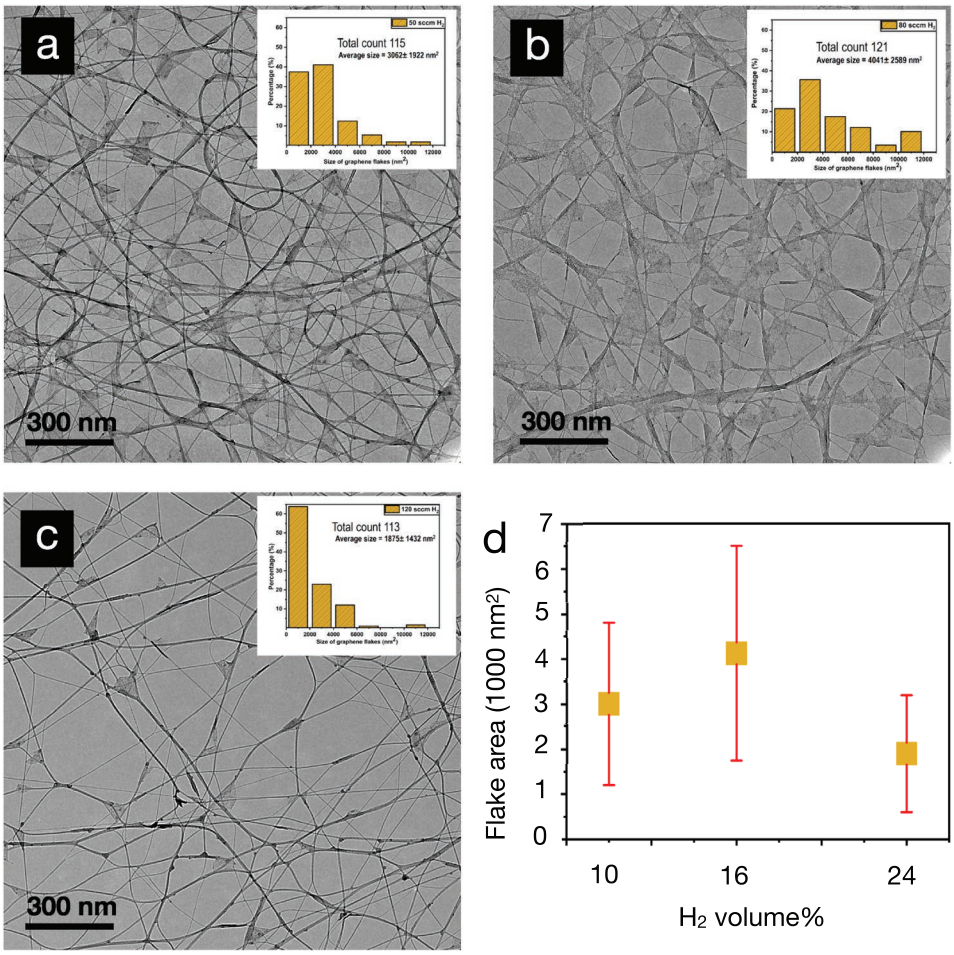

Figure 4. The effect of hydrogen supply on graphene formation. a–c) TEM overview images showing, at respective order, the density of graphene flakes formed at 10, 16, and 24 vol% H_2 content. The insets show histograms of the flake surface area and the average values with uncertainties corresponding to one standard deviation are compared in (d).

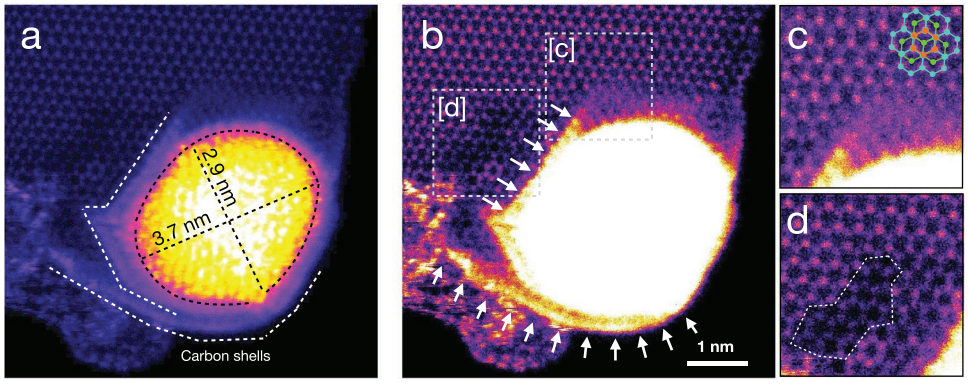

Figure 5. The catalyst-graphene interface. a–b) A graphene flake attached to a carbon shell partially encapsulating an iron catalyst particle. The image was acquired with the MAADF detector in STEM and is reproduced with two different contrast settings to highlight the carbon and iron contents separately. The subpanel c) magnifies the top part where the carbon shell seems to attach to graphene. The varying brightness of the graphene atoms is a result of ABA-stacked triple layer, as is schematically overlaid in the top right corner. d) An area that is most likely graphene monolayer near the catalyst particle. The contrast was enhanced by applying the ImageJ lookup table "fire."

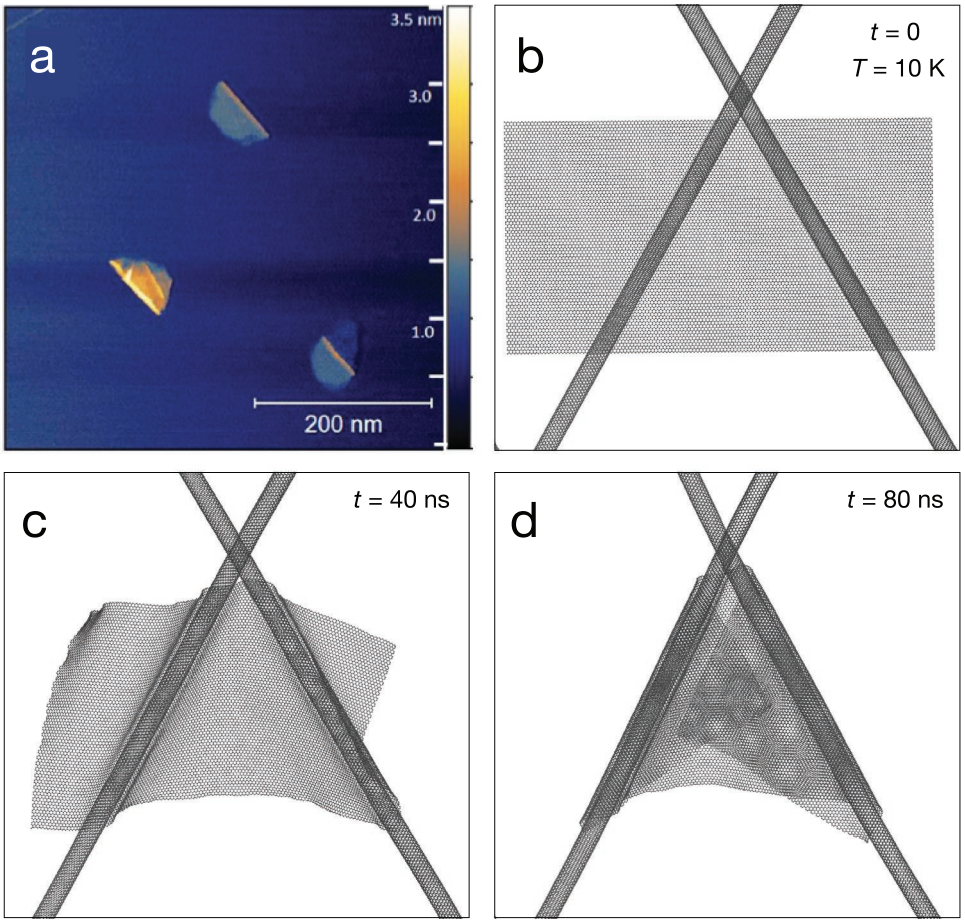

Figure 6. a) Isolated graphene flakes on mica imaged with an atomic force microscope. The thickness of the flakes varies from 1–5 layers. b–d) Snapshots taken at 40 ns intervals of a vdW wrapping of a graphene monolayer around a pair of crossed (10,10) SWCNTs. The process takes place even at 10 K temperature.

thermophoresis.[39] A few spatially separated graphene flakes are shown in **Figure 6**a (and more can be found from Figure S11, Supporting Information). The morphology of the flakes, although without SWCNT support, resembles that of the "axes" earlier characterized by STEM. The apparent bilayer configuration could be a result of, for example, thermal fluctuations stabilized by folding, interactions with the substrate during deposition, or even the equilibrium configuration they grow in. The myriad folding configurations seen in the STEM experiments, however, are probably a result of gas-phase collisions. These can occur both during synthesis or deposition as we have earlier demonstrated for nanotube bundle formation.[35] To analyze the concept of gas-phase folding we studied the dynamics by atomistic simulations (see Section 4). A 30.50 nm × 16.50 nm graphene sheet was brought to a distance of 0.8 nm from a pair of crossed (10,10) nanotubes and the model was allowed to relax without any constraints until the forces were below 0.5×10^{-4} eV per AA. To describe the system, we used the adaptive intermolecular reactive empirical bond order (AIREBO)[57] potential for covalent bonds, augmented with a Morse potential[58] to include vdW interactions. Commensurate with our earlier study, the molecular orbital torsion flag in AIREBO was disabled.[16] The temperature in the simulation cell was 10 K.

Snapshots taken at 40 ns intervals are shown in Figures 6b–d and the video in the Supporting Information. A sail-configuration forms immediately upon molecules reaching the vdW distance at the collision point. Folding was assisted by thermal fluctuations (at 0 K the structures remained frozen) and proceeded rapidly once initiated, minimizing the surface energy, resulting in a covalent structure that becomes distorted.

Finally, the question remains why some structures emerge as graphene and others as SWCNTs or fullerenes. The MD simulations provide one plausible explanation. It is possible that, at a favorable H:C stoichiometry, hexagonal carbon fragments could form in the gas-suspension. These fragments, while perhaps not thermodynamically stable in themselves, could become covalently incorporated into the sp^2 carbon embryos on the catalyst particles.[49] From thereon, depending on the internal morphology and number concentration of the fragments, further polymerization reactions could lead into different allotropes with a distinct statistical prevalence, as sketched in **Figure 7**. For example, if only fragments with a small radius of curvature (i.e., rich in pentagon defects) were to be incorporated into the system that is simultaneously supplied by catalytic decomposition of hydrocarbons on the particle, it would likely evolve towards the fullerite conformation. This could further lead the formation

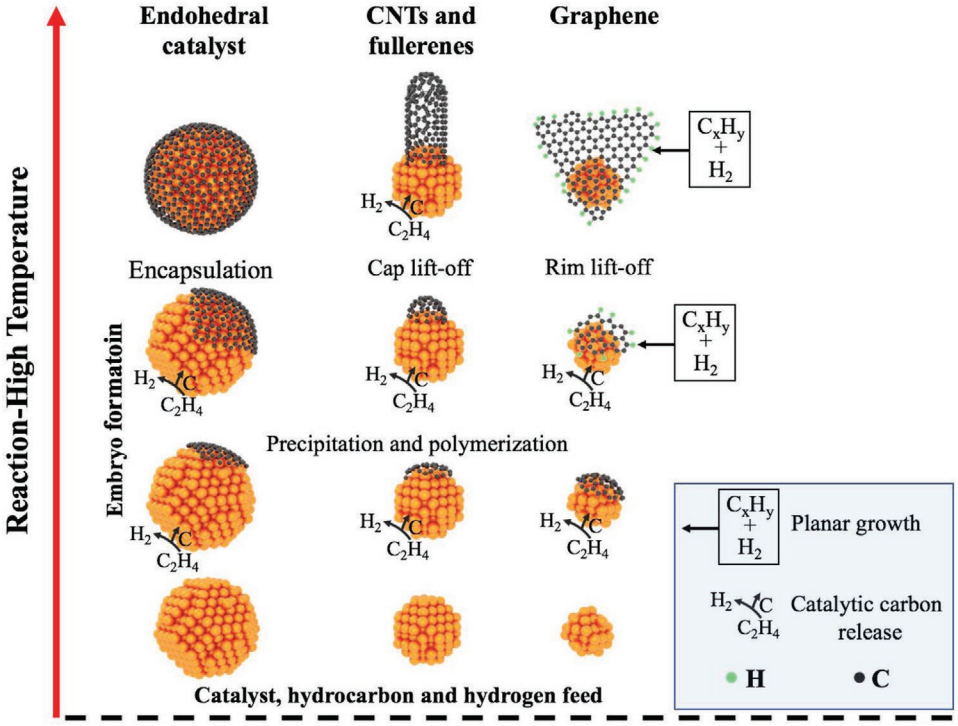

Figure 7. The formation of low-dimensional carbon allotropes in gas-suspension. Possible reaction trajectories for the formation of endohedral catalysts (left), carbon nanotubes and fullerenes (center), and graphene (right). All allotropes nucleate from the catalysts, but depending on particle diameter and the defects in the carbon fragments (see Figure 3), growth proceeds along different paths. After the nucleation, the carbon fragments may detach themselves from the catalyst and further grow through chain polymerization of active carbon species in the gas-phase.

of fullerenes or carbon nanotubes, of which the latter outcome requires the rim of the embryo to become anchored on the particle, as has been shown via MD simulations and observed in in situ electron microscopy experiments.[19,59,60] This is depicted in the center column of Figure 7.

The incorporation of planar fragments could, accordingly, initiate a chain of events that leads into the formation of graphene. We suspect that this process is only feasible on small catalyst particles, where bending the C—C bonds with a sufficient amount to accommodate to the particle's radius of curvature would be too costly in terms of energy, and hence the growth proceeds in a planar configuration eventually forming the graphene embryo. At this point the new-born graphene may detach[61] from the catalyst and its size, while suspended in the gas-phase, increases through the chain polymerization and self-pyrolytic decomposition of active carbon species near the edges. This is depicted on the right side of Figure 7. This idea is also supported by our experimental results, which indicates that the average size of the catalysts is inversely proportional to the rate of graphene formation. Increasing the particle diameter from 2 to 5 nm essentially mitigated the graphene growth with intermediate steps in between, while at the same time SWCNTs formed in relatively large quantities (see Figure S7, Supporting Information). It thus appears that on larger catalyst the carbon fragments more readily follow the surface of the particle to encapsulate the catalyst inside endohedral fullerene shells[19] as depicted on the left side of Figure 7.

Finally, it is worth noting that the formation of graphene in microwave plasma reported by Dato et al. did not require a catalyst.[32] In those experiments, also no hydrogen supply other than that released from the alcohol vapor was needed. However, conditions at the extreme plasma temperatures of 3000–4000 K are entirely different from those in our CVD process, prohibitive for example for the H—C bond formation. It is thus likely that in their experiments the graphene was in fact formed at the plasma boundary-layer where the energetics would allow a process more similar to that observed in our MD simulations. Charged ions escaping at the boundary-layer at energies frequently higher than 25 eV would also explain the defectiveness of their graphene.[62] In our experiments the most critical factor for graphene formation seemed to be the H:C stoichiometry, which is a temperature dependent growth parameter. Although not extensively discussed here, besides C_2H_4, graphene was also synthesized from ethanol (C_2H_5OH) and methane (CH_4) by slightly adjusting the H_2 concentration (see Table S1, Supporting Information). Changing the catalyst metal from Fe to cobalt (Co) to nickel (Ni) to Co–Ni alloy did not change the overall result, despite the fact that their respective catalytic activities affected the overall production yield. This result underlines the irrelevance of the catalyst which appears to be nothing more than a nucleation site for the graphitic carbon formation.

3. Conclusion

In conclusion, we have demonstrated a chemical vapor deposition process in which high-quality graphene, SWCNTs, and fullerenes were simultaneously produced in the gas phase.

Based on the evidence accumulated in atomically resolved transmission electron microscopic experiments and molecular dynamics simulations, we postulate that the formation of gas-suspended, hexagonal carbon fragments is instrumental to the formation of graphene nucleated by nanometer-sized catalyst clusters. We further believe that the stability of the emerging 2D graphene flakes is determined by the equilibrium of carbon–hydrogen stoichiometry through mitigation of topological defects, and by synthesis temperature. The proposed method provides a previously unexplored gas-phase route to the fabrication and dry deposition of graphene-based hybrid thin film materials.

4. Experimental Section

Material Synthesis: The materials were primarily synthesized by using iron (Fe) catalyst particles. These catalysts were formed through physical evaporation (and subsequent nucleation) of a pair of Fe electrodes by low-energy spark discharges created by applying 2–3 kV potential across a gap in between them.[63] Nitrogen was used as a particle carrier gas (N_2 99.995% purity), introducing them into a vertical CVD reactor. The flow rates were adjusted to sum to 0.5 slpm, which contained 0.36–0.44 slpm of N_2 depending on other conditions. Low-dimensional carbon was formed in the CVD reactor[30,34] from 0.1×10^{-3} slpm (200 ppm in volume) of ethylene (C_2H_4) (99.999% from AGA). The synthesis mediator was hydrogen gas (H_2, 99.999% from AGA) having respective flow rates of 0.13–0.05 slpm. The CVD reactor temperature was kept at 1050 °C. The residence time in the growth region (800–1050 °C) was ≈10 s. In some experiments, 0.01 slpm of hydrogen sulfide (H_2S, 99.999% from AGA) diluted down to 100 ppm in N_2 was used as a growth promoter. However, this procedure was not instrumental for the synthesis but was helpful for maintaining a long-term stability of the process.

Synthesis was also tested using catalyst formed by the thermal decomposition of ferrocene vapor (Fe-$FeCp_2$) inside the CVD reactor. These tests also included different carbon sources, mainly ethylene, methane, and ethanol. A description of these methods can be found in references[64,65] and a brief summary of the different conditions used are provided in Table S1, Supporting Information.

Sample Characterizations—Transmission Electron Microscopy: The atomic resolution scanning transmission electron microscopy experiments were conducted using an aberration-corrected Nion UltraSTEM 100 operated with a 60 keV primary beam energy with a pressure of 5×10^{-10} mbar at the sample. The electrons were detected with a medium angle annular dark field detector (MAADF) with a semi-angle of 60–200 mrad.

The electron diffraction patterns and TEM images in Supporting Information were acquired with a double-corrected JEOL JEM2200 high-resolution transmission electron microscope at 80 keV primary beam energy. The area of interests was selected by inserting a 0.17 µm selected area aperture in the beam path.

Sample Characterizations—Spectroscopic Measurements: Optical absorption spectra (data in Supporting Information) were measured using an Agilent Carry 5000 UV–vis–NIR spectrometer from Agilent Technologies. The Raman spectra were acquired with a Horiba Labram-HR 800 Raman spectrometer from Horiba Jobin-Yvon using excitation wavelength of 632.8 nm and ≈1 µm laser spot size.

Sample Characterizations—Atomic Force Microscopy: The atomic force microscopic observations were conducted with Veeco Dimensions 5000 unit from Bruker nano surfaces Inc operate in tapping mode. The samples were directly accumulated on cleaved muscovite mica (V-4 grade electron microscopy sciences, U.S.A.) substrate using thermophoresis.

Sample Characterizations—Molecular Dynamics Simulations: Each simulation was a continuation of one of ten unique trajectories initially containing exactly 100 C_2H_4 molecules in a cubic simulation cell with a side length of 3 nm. The different H:C ratios in the simulation were achieved by at random removing a total of 80 H atoms from the initial configuration at 5 ps intervals. Thus, a total of 60 unique reaction trajectories were generated. The temperature within the simulation cell was set to 1050 °C. Newton's laws of motion were integrated using the velocity–Verlet algorithm[66] with a time step of 1.0 fs. The furnace temperature of 1050 °C was enforced via an NVT ensemble using a Nose–Hoover chain thermostat.[67] The SCC-DFTB method[68] with the trans3d-0-1 parameter set[69] and a finite electronic temperature of 10 000 K[70,71] was used to iteratively calculate the quantum chemical potential energy and energy gradients. The influence of the H:C ratio during these processes was specifically investigated, by varying the hydrogen content during the simulation to varying degrees, following other reports.[46,48,72–74] Full details of these simulations are provided in the Supporting Information.

Sample Characterizations—vdW Atomistic Simulations: Graphene folding on SWCNTs was energy optimized with AIREBO potential augmented with Morse potential for vdW interactions. The torsion flag for molecular orbitals was disabled, which best matched with our earlier experimental results.[16] The model system consisted of a 30.50 nm × 16.50 nm graphene sheet brought to a distance of 0.8 nm from a pair of crossed (10,10) nanotubes. The cell size was a 96.6 nm triclinic cell where, to achieve periodic boundary conditions, four nanotubes were crossed by 60° angles.

Supporting Information

Supporting Information is available from the Wiley Online Library or from the author.

Acknowledgements

The research described here received funding from European Union Seventh Framework Program under Grant Agreement No. 604472 (IRENA project), and the Aalto Energy Efficiency (AEF) Research Program through the MOPPI project. The research has also been partially supported by Academy of Finland via projects 286546 (DEMEC), 316572 (CNTstress) and 292600 (SUPER) as well as by TEKES Finland via projects 3303/31/2015 (CNT-PV) and 1882/31/2016 (FEDOC). The authors also thank the Austrian Science Fund (FWF) for funding under project no. I3181-N36. S.A acknowledges funding from HEAL department Khyber Pakhtunkhwa, Pakistan through SO(Trg)HE/1-10/Ph.D scholarships/2012. A.G.N. acknowledges RFBR for financial support (project number 20-03-00804). This work made use of the Aalto University Nanomicroscopy Center facilities. The authors thank Dr. Mirkka Jones and Dr. Bernadette Gehl-Väisänen for proofreading.

Conflict of Interest

The authors declare no conflict of interest.

Author contributions

S.A., Q.Z., and E.I.K. proposed the project idea. S.A. designed and performed the main experiments. A.H., E.-X.D., Y.L., and A.G.N. participated in the FC-CVD synthesis and deposition. S.A., K.M., H.J., J.K. and A.T.K., participated in the characterization of the material. S.A., K.M., N.W., and B.M. participated in the figure processing and manuscript preparation. B.M., A.J.P., and M. R.A. M. ran the simulations.

Keywords

dry-deposition, floating catalyst CVD, graphene growth, low-dimensional carbon allotropes

Received: June 13, 2020
Revised: August 16, 2020
Published online: September 13, 2020

[1] K. S. Novoselov, A. K. Geim, S. V. Morozov, D. Jiang, Y. Zhang, S. V. Dubonos, I. V. Grigorieva, A. A. Firsov, *Science.* **2004**.
[2] P. R. Wallace, *Phys. Rev.* **1947**.
[3] K. Kaiser, L. M. Scriven, F. Schulz, P. Gawel, L. Gross, H. L. Anderson, *Science* **2019**.
[4] P. R. Buseck, S. J. Tsipursky, R. Hettich, *Science* **1992**.
[5] S. Iijima, T. Ichihashi, *Nature* **1993**, *363*, 603.
[6] J. Baringhaus, M. Ruan, F. Edler, A. Tejeda, M. Sicot, A. Taleb-Ibrahimi, A. P. Li, Z. Jiang, E. H. Conrad, C. Berger, C. Tegenkamp, W. A. De Heer, *Nature* **2014**.
[7] Y. Cao, V. Fatemi, S. Fang, K. Watanabe, T. Taniguchi, E. Kaxiras, P. Jarillo-Herrero, *Nature* **2018**.
[8] F. Wu, S. Das Sarma, *Phys. Rev. Lett.* **2020**.
[9] W. Bao, L. Jing, J. Velasco, Y. Lee, G. Liu, D. Tran, B. Standley, M. Aykol, S. B. Cronin, D. Smirnov, M. Koshino, E. McCann, M. Bockrath, C. N. Lau, *Nat. Phys.* **2011**.
[10] A. K. Geim, I. V. Grigorieva, *Nature* **2013**.
[11] F. Simon, M. Monthioux, *Carbon Meta-Nanotubes*, John Wiley and Sons, New York **2011**.
[12] K. Kim, T. H. Lee, E. J. G. Santos, P. S. Jo, A. Salleo, Y. Nishi, Z. Bao, *ACS Nano* **2015**.
[13] J. Zhang, Y. Wei, F. Yao, D. Li, H. Ma, P. Lei, H. Fang, X. Xiao, Z. Lu, J. Yang, J. Li, L. Jiao, W. Hu, K. Liu, K. Liu, P. Liu, Q. Li, W. Lu, S. Fan, K. Jiang, *Adv. Mater.* **2017**.
[14] D. Jariwala, T. J. Marks, M. C. Hersam, *Nat. Mater.* **2017**, *16*, 170.
[15] A. Chuvilin, U. Kaiser, E. Bichoutskaia, N. A. Besley, A. N. Khlobystov, *Nat. Chem.* **2010**.
[16] K. Mustonen, A. Hussain, C. Hofer, M. R. A. Monazam, R. Mirzayev, K. Elibol, P. Laiho, C. Mangler, H. Jiang, T. Susi, E. I. Kauppinen, J. Kotakoski, J. C. Meyer, *ACS Nano* **2018**.
[17] A. G. Nasibulin, P. V. Pikhitsa, H. Jiang, D. P. Brown, A. V. Krasheninnikov, A. S. Anisimov, P. Queipo, A. Moisala, D. Gonzalez, G. Lientschnig, A. Hassanien, S. D. Shandakov, G. Lolli, D. E. Resasco, M. Choi, D. Tománek, E. I. Kauppinen, *Nat. Nanotechnol.* **2007**.
[18] R. J. Nicholls, J. Britton, S. S. Meysami, A. A. Koós, N. Grobert, *Chem. Commun.* **2013**.
[19] L. Zhang, M. He, T. W. Hansen, J. Kling, H. Jiang, E. I. Kauppinen, A. Loiseau, J. B. Wagner, *ACS Nano* **2017**.
[20] Z. Liu, Y. C. Lin, C. C. Lu, C. H. Yeh, P. W. Chiu, S. Iijima, K. Suenaga, *Nat. Commun.* **2014**.
[21] F. Ding, A. R. Harutyunyan, B. I. Yakobson, *Proc. Natl. Acad. Sci. U. S. A.* **2009**.
[22] V. I. Artyukhov, E. S. Penev, B. I. Yakobson, *Nat. Commun.* **2014**.
[23] F. Yang, X. Wang, D. Zhang, J. Yang, D. Luo, Z. Xu, J. Wei, J. Q. Wang, Z. Xu, F. Peng, X. Li, R. Li, Y. Li, M. Li, X. Bai, F. Ding, Y. Li, *Nature* **2014**.
[24] S. Zhang, L. Kang, X. Wang, L. Tong, L. Yang, Z. Wang, K. Qi, S. Deng, Q. Li, X. Bai, F. Ding, J. Zhang, *Nature* **2017**.
[25] J. Sun, Y. Nam, N. Lindvall, M. T. Cole, K. B. Kenneth, Y. W. Park, A. Yurgens, *Appl. Phys. Lett.* **2014**.
[26] C. M. Seah, S. P. Chai, A. R. Mohamed, *Carbon N. Y.* **2014**.
[27] Y. Magnin, H. Amara, F. Ducastelle, A. Loiseau, C. Bichara, *Science* **2018**.
[28] K. V. Bets, E. S. Penev, B. I. Yakobson, *ACS Nano* **2019**.
[29] M. He, H. Jiang, B. Liu, P. V. Fedotov, A. I. Chernov, E. D. Obraztsova, F. Cavalca, J. B. Wagner, T. W. Hansen, I. V. Anoshkin, E. A. Obraztsova, A. V. Belkin, E. Sairanen, A. G. Nasibulin, J. Lehtonen, E. I. Kauppinen, *Sci. Rep.* **2013**.
[30] S. Ahmad, Y. Liao, A. Hussain, Q. Zhang, E.-X. Ding, H. Jiang, E. I. Kauppinen, *Carbon N. Y.* **2019**.
[31] Y. Liao, H. Jiang, N. Wei, P. Laiho, Q. Zhang, S. A. Khan, E. I. Kauppinen, *J. Am. Chem. Soc.* **2018**.
[32] A. Dato, V. Radmilovic, Z. Lee, J. Phillips, M. Frenklach, *Nano Lett.* **2008**.
[33] Y. C. Choi, Y. M. Shin, Y. H. Lee, B. S. Lee, G. S. Park, W. B. Choi, N. S. Lee, J. M. Kim, *Appl. Phys. Lett.* **2000**.
[34] S. Ahmad, E.-X. Ding, Q. Zhang, H. Jiang, J. Sainio, M. Tavakkoli, A. Hussain, Y. Liao, E. I. Kauppinen, *Chem. Eng. J.* **2019**, *378*, 122010.
[35] K. Mustonen, P. Laiho, A. Kaskela, T. Susi, A. G. Nasibulin, E. I. Kauppinen, *Appl. Phys. Lett.* **2015**.
[36] D. R. Chen, D. Y. H. Pui, D. Hummes, H. Fissan, F. R. Quant, G. J. Sem, *J. Aerosol Sci.* **1998**.
[37] M. Adachi, K. Okuyama, *Aerosol Sci. Technol.* **1985**.
[38] A. Kaskela, A. G. Nasibulin, M. Y. Timmermans, B. Aitchison, A. Papadimitratos, Y. Tian, Z. Zhu, H. Jiang, D. P. Brown, A. Zakhidov, E. I. Kauppinen, *Nano Lett.* **2010**.
[39] P. Laiho, K. Mustonen, Y. Ohno, S. Maruyama, E. I. Kauppinen, *ACS Appl. Mater. Interfaces* **2017**.
[40] K. Mustonen, P. Laiho, A. Kaskela, Z. Zhu, O. Reynaud, N. Houbenov, Y. Tian, T. Susi, H. Jiang, A. G. Nasibulin, E. I. Kauppinen, *Appl. Phys. Lett.* **2015**, *107*, 013106.
[41] M. Tripathi, A. Mittelberger, K. Mustonen, C. Mangler, J. Kotakoski, J. C. Meyer, T. Susi, *Phys. Status Solidi—Rapid Res. Lett.* **2017**, *11*, 1700124.
[42] L. Liu, H. Zhou, R. Cheng, W. J. Yu, Y. Liu, Y. Chen, J. Shaw, X. Zhong, Y. Huang, X. Duan, *ACS Nano* **2012**.
[43] R. Mirzayev, K. Mustonen, M. R. A. Monazam, A. Mittelberger, T. J. Pennycook, C. Mangler, T. Susi, J. Kotakoski, J. C. Meyer, *Sci. Adv.* **2017**.
[44] F. Banhart, J. Kotakoski, A. V. Krasheninnikov, *ACS Nano* **2011**, *5*, 26.
[45] H. Inani, K. Mustonen, A. Markevich, E. X. Ding, M. Tripathi, A. Hussain, C. Mangler, E. I. Kauppinen, T. Susi, J. Kotakoski, *J. Phys. Chem. C* **2019**.
[46] H. B. Li, A. J. Page, S. Irle, K. Morokuma, *J. Phys. Chem. Lett.* **2013**.
[47] B. Saha, S. Irle, K. Morokuma, *J. Chem. Phys.* **2010**.
[48] B. Saha, S. Shindo, S. Irle, K. Morokuma, *ACS Nano* **2009**.
[49] Y. Wang, X. Gao, H. J. Qian, Y. Ohta, X. Wu, G. Eres, K. Morokuma, S. Irle, *Carbon N. Y.* **2014**.
[50] I. Mitchell, A. J. Page, *Carbon N. Y.* **2018**.
[51] S. Irle, G. Zheng, Z. Wang, K. Morokuma, *J. Phys. Chem. B* **2006**.
[52] G. Zheng, Z. Wang, S. Irle, K. Morokuma, *J. Nanosci. Nanotechnol.* **2007**.
[53] Y. Yao, C. Feng, J. Zhang, Z. Liu, *Nano Lett.* **2009**.
[54] M. P. Ruiz, A. Callejas, A. Millera, M. U. Alzueta, R. Bilbao, *J. Anal. Appl. Pyrolysis* **2007**.
[55] A. Moisala, A. G. Nasibulin, E. I. Kauppinen, *J. Phys. Condens. Matter* **2003**.
[56] A. Hussain, *Nanoscale* **2020**.
[57] D. W. Brenner, *Phys. Rev. B* **1990**.
[58] T. C. O'Connor, J. Andzelm, M. O. Robbins, *J. Chem. Phys.* **2015**.
[59] M. Picher, P. A. Lin, J. L. Gomez-Ballesteros, P. B. Balbuena, R. Sharma, *Nano Lett.* **2014**.
[60] R. Rao, R. Sharma, F. Abild-Pedersen, J. K. Nørskov, A. R. Harutyunyan, *Sci. Rep.* **2014**.
[61] M. Diarra, A. Zappelli, H. Amara, F. Ducastelle, C. Bichara, *Phys. Rev. Lett.* **2012**.
[62] O. Lehtinen, J. Kotakoski, A. V. Krasheninnikov, A. Tolvanen, K. Nordlund, J. Keinonen, *Phys. Rev. B—Condens. Matter Mater. Phys.* **2010**.

[63] S. Ahmad, P. Laiho, Q. Zhang, H. Jiang, A. Hussain, Y. Liao, E. X. Ding, N. Wei, E. I. Kauppinen, *J. Aerosol Sci.* **2018**, *123*, 208.
[64] E.-X. Ding, *Nanoscale* **2017**, *9*, 17601.
[65] A. Hussain, Y. Liao, Q. Zhang, E. X. Ding, P. Laiho, S. Ahmad, N. Wei, Y. Tian, H. Jiang, E. I. Kauppinen, *Nanoscale* **2018**.
[66] W. C. Swope, H. C. Andersen, P. H. Berens, K. R. Wilson, *J. Chem. Phys.* **1982**.
[67] S. Nosé, *J. Chem. Phys.* **1984**.
[68] M. Elstner, D. Porezag, G. Jungnickel, J. Elsner, M. Haugk, T. Frauenheim, *Phys. Rev. B—Condens. Matter Mater. Phys.* **1998**.
[69] G. Zheng, H. A. Witek, P. Bobadova-Parvanova, S. Irle, D. G. Musaev, R. Prabhakar, K. Morokuma, M. Lundberg, M. Elstner, C. Köhler, T. Frauenheim, *J. Chem. Theory Comput.* **2007**.
[70] M. Weinert, J. W. Davenport, *Phys. Rev. B* **1992**.
[71] R. M. Wentzcovitch, J. L. Martins, P. B. Allen, *Phys. Rev. B* **1992**.
[72] C. A. Eveleens, A. J. Page, *Nanoscale* **2017**.
[73] J. Wang, Q. Wang, W. She, C. Xie, X. Zhang, M. Sun, J. Xiao, S. Wang, *J. Power Sources* **2019**.
[74] B. McLean, G. B. Webber, A. J. Page, *J. Am. Chem. Soc.* **2019**.